Ligament formation in sheared liquid-gas layers

Thomas Boeck[1], Jie Li[2], Enrique López-Pagés[3], Philip Yecko [4] and Stéphane Zaleski[5]

1. Fachgebiet Thermo- und Fluiddynamik, TU Ilmenau,
P.O. Box 100565, 98684 Ilmenau, Germany
2. Department of Engineering, University of Cambridge, Trumpington Street
Cambridge CB2 1PZ, U.K.
3. Fluid Mechanics Department, Universidad de Zaragoza, 50015 Zaragoza,
España
4. Department of Mathematical Sciences, Montclair State University, Montclair,
NJ 07043 USA
5. Laboratoire de Modélisation en Mécanique,
CNRS and Université Pierre et Marie Curie (Paris VI), 4 place Jussieu, 75005
Paris, France,
email: zaleski@lmm.jussieu.fr

Abstract

We perform numerical simulations of two-phase liquid-gas sheared layers, with the objective of studying atomization. The Navier-Stokes equations for two-dimensional incompressible flow are solved in a periodic domain. A Volume of Fluid (VOF) method is used to track the interface. The density ratio is kept around 10. The calculations show good agreement with a fully viscous Orr-Sommerfeld linear theory over several orders of magnitude of interface growth. The nonlinear development shows the growth of finger-like structures, or ligaments, and the detachment of droplets. The effect of the Weber and Reynolds numbers, the boundary layer width and the initial perturbation amplitude are discussed through a number of typical cases. Inversion of the liquid boundary layer is shown to yield more readily ligaments bending upwards and thus more likely to produce droplets.

1 Introduction

A strong gas flow parallel to a liquid-gas interface tends to shatter it into small droplets. Wind, when of enough magnitude, will strip droplets from wave crests. Many industrial atomization processes rely on the atomization of fast liquid jets into droplets. This spray formation process is of considerable importance in combustion technology. A case in point is air-blast atomization devices (Lefebvre, 1989) or coaxial injectors in cryogenic engines.

Our current understanding of the mechanisms leading to atomization rests in part on various theoretical approaches and in part on experimental observation. In addition there are relatively few numerical studies (Tauber & Tryggvason, 2002; Tauber *et al.*, 2002; Leboissetier & Zaleski, 2002). The work reported here focuses on the influence of viscosity on ligament formation and sizes. Various mechanisms have been suggested to explain liquid jet atomization (Reitz & Bracco, 1982; Lasheras & Hopfinger, 2000). At low enough Weber number (defined below) the Savart-Plateau-Rayleigh jet instability dominates and creates droplets of roughly the size of the jet. At larger velocities, instabilities of much shorter length scale develop.

At these large speeds, the process is rather complex. It involves turbulence upstream of the injector as argued by Faeth *et al.* (1995), instabilities near the injector due to the shearing motion of the liquid and the gas, ligament and droplet formation and dispersion in an initially dense spray. The region near the nozzle, where spray formation is initiated by the growth of surface instabilities is thus especially interesting. To understand the instabilities that develop in this region we focus in this paper on the two-dimensional, spatially-periodic shear flow. This simplification is warranted by the approximately periodic nature of the flow observed in experiments (see for instance Hoyt & Taylor (1977); Lasheras & Hopfinger (2000)).

There is a large literature on the linear theory of the instability. The classical stability theory of Chandrasekhar (1961) predicts droplet formation when the gas Weber number We (defined below) exceeds a critical value. One effect of viscosity is also to impose the existence of a critical Reynolds number for instability development. Recently, we have discussed in another paper (Yecko *et al.*, 2002) the full viscous stability theory, finding several distinct modes of instability. Relatively little work on the other hand can be found on the nonlinear development. Inviscid fluid equations were solved by Rangel & Sirignano (1988) using a boundary integral method for relatively moderate density ratios $r = \rho_g/\rho_l$, however despite the large Reynolds numbers at which atomization occurs, it is likely that finite viscosity effects are present and thus inviscid fluid flow may not be close to Navier Stokes solutions.

Full simulations of the Navier-Stokes equations for two-phase liquid-gas layers were seldom performed. Our group has performed calculations using Volume of Fluid (VOF) methods. Some preliminary two-dimensional results may be found in Keller *et al.* (1994), Li (1995) and Leboissetier & Zaleski (2002) , while Zaleski *et al.* (1995) , Zaleski *et al.* (1996) and Bianchi *et al.* (2005) have shown some preliminary three-dimensional results. Agreement between the volume of fluid calculations and linear theory is particularly difficult to obtain, because of the complex effect of viscosity on the base profile and on the instability growth rates and modes. Recently two and three-dimensional solutions of the full Navier-Stokes equations were performed by interface tracking methods, using connected markers to follow the interface (Tauber & Tryggvason, 2002; Tauber *et al.*, 2002).

In this paper we focus on the effect of viscosity on the length scales of the ligaments and droplets. The theories existing today for droplet size (see Lasheras & Hopfinger (2000) for a review and Marmottant & Villermaux

(2002) for recent results) all assume that the droplet size is in proportion of the wavelength of the instability. However in this paper we fix the wavelength of the instability and observe the variation in droplet sizes. This should lead to improved theories for droplet formation.

2 Basic equations and numerical method

We model the problem assuming sharp interfaces between two Newtonian, viscous fluids with constant surface tension, in two dimensions of space. This leads to the Navier-Stokes equations. We note $\mathbf{u}(\mathbf{x}, t)$, $p(\mathbf{x}, t)$ the velocity and pressure field, σ the surface tension (assumed constant), κ the interface curvature, $\mathbf{n}$ the normal to the interface, μ the viscosity. The equations are

$$\partial_t \mathbf{u} + \mathbf{u} \cdot \nabla \mathbf{u} = -\frac{1}{\rho} \nabla p + \frac{1}{\rho} \nabla \cdot (2\mu \mathbf{D}) + \sigma \kappa \mathbf{n} \delta_S, \tag{1}$$

where δ_S is a distribution concentrated on the interface and $\mathbf{D}$ is the rate-of-strain tensor

$$D_{ij} = \frac{1}{2} \left(\frac{\partial u_j}{\partial x_i} + \frac{\partial u_i}{\partial x_j} \right). \tag{2}$$

Incompressible flow is assumed

$$\nabla \cdot \mathbf{u} = 0. \tag{3}$$

The interface follows the flow, or in other words, the normal velocity of the interface equals the normal flow velocity $\mathbf{u} \cdot \mathbf{n}$. For an interface height $h(x, t)$ this implies

$$\partial_t h = v - u \partial_x h \tag{4}$$

The viscosity and density are constant in each phase but vary from phase to phase. An important consequence of Eq. (1) are the jump conditions on the interface:

$$[\mathbf{u}]_S = 0 \tag{5}$$

for the velocity and

$$[-p\mathbf{n} + 2\mu\mathbf{n}\cdot\mathbf{D}]_s = \sigma\kappa\mathbf{n}, \tag{6}$$

for the stress.

The equations are solved in a square $L \times L$ domain and periodic boundary conditions are used in the x direction. In the y direction we use free-slip boundary conditions so that $v = 0$ and $\partial_y u = 0$. To fully specify the problem we also need initial conditions. The initial base flow is described in Sections 3 and 4. To this base flow we add an initial perturbation $\epsilon\mathbf{u}_1(\mathbf{x}, 0)$ where ϵ is some small number.

With periodic boundary conditions, the problem is invariant under any Galilean transformation that shifts the horizontal velocity field. Thus the only relevant velocity scale is the velocity difference ΔU. With the above parameters several dimensionless numbers may be defined, such as the Weber numbers $\mathrm{We}_i = \rho_i(\Delta U)^2 L/\sigma$ based on the gas ($i = g$) or the liquid ($i = l$) and similarly the Reynolds numbers $\mathrm{Re}_i = \rho_i \Delta U L/\mu_i$. Two additional numbers are the density and viscosity ratios $r = \rho_g/\rho_l = \mathrm{We}_g/\mathrm{We}_l$ and $k = \nu_g/\nu_l = \mathrm{Re}_l/\mathrm{Re}_g$. With for instance $\mathrm{We}_g, \mathrm{Re}_g, r$ and k we have a full set of parameters.

We solve these equations using a combination of numerical methods described in several prior publications (Lafaurie *et al.*, 1994; Li, 1995; Gueyffier *et al.*, 1999; Scardovelli & Zaleski, 1999). The flow in the gas and liquid is considered as the flow of a single fluid with variable viscosity and density, and with singular forces inside the domain, in a manner consistent with the formulation used in equation (1). We then discretize directly equation (1) on a square, staggered, finite-difference grid known as the Marker-and-Cell (MAC) grid. An explicit projection method is used for the pressure. This method requires the resolution of an elliptic equation for the pressure which is solved using a multigrid method. The multigrid resolution is made more efficient by tuning the number of iterations of the smoothing operator. The tuning is a function of the convergence rate.

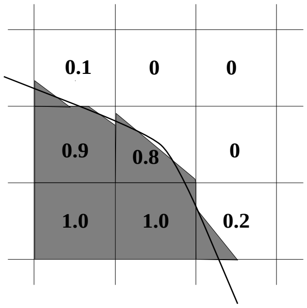

Figure 1: The basic principle of the VOF-PLIC method: the interface is reconstructed by linear unconnected segments in each cell.

The motion of the interface following the flow is tracked using a second-order volume of fluid (VOF) method described in Li (1995); Gueyffier *et al.* (1999). The interface is located by a Volume of Fluid function C_{ij}, and is reconstructed at each time step as a series of linear segments (Fig. 1). The principal advantage of this method compared to its competition is that it ensures very good volume conservation. To transport the interface segments from cell to cell we use the "explicit lagrangian" method Li (1995); Scardovelli & Zaleski (2003); Aulisa *et al.* (2003) . It conserves mass with acceptable accuracy (better that 0.1%) and automatically breaks thin ligaments.

For the viscosity of mixed cells we used two methods. The first method is the arithmetic mean

$$\mu_{ij} = \mu_1 C_{ij} + \mu_2 (1 - C_{ij}) \tag{7}$$

where μ_p is the viscosity of phase p and μ_{ij} the viscosity at location ij. When the viscosity is needed at staggered grid locations averages of neighboring points are taken. The other method is the harmonic mean

$$\mu_{ij}^{-1} = \mu_1^{-1} C_{ij} + \mu_2^{-1}(1 - C_{ij}). \tag{8}$$

The arithmetic mean is optimal in a shear flow when the interface is perpendicular to the flow, while the harmonic mean is optimal when the interface is parallel to the flow.

Surface tension is also represented using an approximation of the distribution δ_S in (1) over the grid. We use the "continuous surface stress" formulation described in Lafaurie *et al.* (1994) in which the surface tension force is represented in a continuous way. The normal is calculated by

$$\mathbf{n} = \frac{\nabla_h\, C}{||\nabla_h C||}. \tag{9}$$

where ∇_h is a finite difference operator. To compute the capillary term we use the identity (valid for constant σ)

$$\sigma\kappa\mathbf{n}\delta_S = \nabla \cdot [\sigma(\mathbf{I} - \mathbf{n} \otimes \mathbf{n})]. \tag{10}$$

We discretize it using

$$\sigma\kappa\mathbf{n}\delta_S = \nabla_h \cdot [\sigma(\mathbf{1} - \mathbf{n}_h \otimes \mathbf{n}_h)||\nabla_h C||] \tag{11}$$

In some cases (discussed below) we replace C by a smoothed field. In the smoothed version the function C_{ij} is filtered to obtain a smoothed function

$$\tilde{C}_{ij} = \frac{1}{2} C_{ij} + \frac{1}{8}[C_{i,j-1} + C_{i,j+1} + C_{i-1,j} + C_{i+1,j}] \tag{12}$$

then we use it in expressions (9) and (11) above. This representation of surface tension was shown to give good results for small amplitude capillary waves. Indeed, simulations and theory compare well for capillary surface oscillations as shown in Gueyffier *et al.* (1999). The smoothing is generally considered to be a useful operation as it reduces spurious currents (Gueyffier *et al.*, 1999) however we show below in Section 4.5 that it may also have drawbacks.

3 Comparison with linear theory

Many previous tests of components of this code were performed, but it had not been possible to succesfully compare the instability growth with linear theory.

A specific test of our code for the study of sheared layers is to compare its predictions to those of linear theory. Conversely, the linear theory is also tested . The linear theory is rather complex and has been worked out in detail only recently by Yecko *et al.* (2002); Boeck & Zaleski (2005); Gordillo & Perez-Saborid (2005). An important conclusion of the recent work is that great care must be taken to resolve the viscous stability problem with the corresponding Orr-Sommerfeld equations, since their growth rates are very different from the inviscid ones. In particular a new "H-mode", named after Hooper and Hinch (Hooper & Boyd, 1983; Hooper, 1985; Hooper & Boyd, 1987; Hinch, 1984) was found at higher wavenumbers and growth rates than the previously known modes. Here we give only the result of the comparison between linear theory and full numerics, for a discussion of the theory and modes the reader is referred to the abvove references.

The typical base flow takes some time to adapt after the nozzle exit but eventually settles on a flow with two boundary layers, one in the gas and the other in the liquid. A realistic base flow that is a solution of the Navier-Stokes equations has been considered (Figure 2(c)). It is made of two error-function profiles with

$$u_{0,i}(y) = U_i \mathrm{erfc}\left(\frac{y}{\delta_i}\right) \tag{13}$$

where the index $i = g$ for $y > 0$ and $i = l$ otherwise. When $\delta_i = \sqrt{4\nu_i(t + t_0)}$ this is the flow that would evolve from the step function profile at $t = -t_0$.

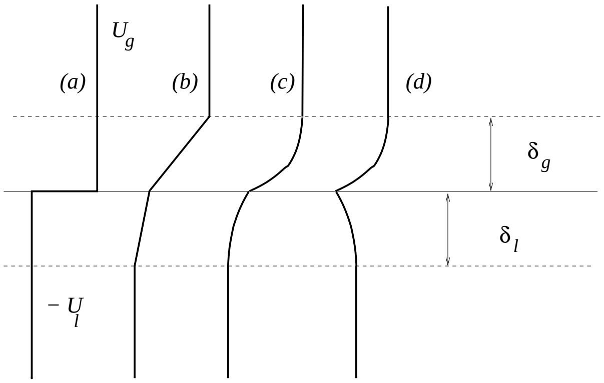

Figure 2: The initial or base flows discussed in this paper (a) The simplest profile: sharp velocity jump (b) A piecewise linear flow with two boundary layers used in early studies. (c) A smooth boundary layers profile, used for comparisons with linear theory and in most full simulations. (d) An inverted liquid boundary layer, which mimics the situation just outside the nozzle.

At $t = 0$ there are two boundary layers of size $\delta_i = \sqrt{4\nu_i t_0}$. Then

$$\delta_g/\delta_l = \sqrt{\nu_g/\nu_l} \tag{14}$$

It is also useful to define numbers based on boundary layer size $Re_g^\star = U_g\delta_g/\nu_g$ and $We_g^\star = \rho_g U_g^2 \delta_g/\sigma$. The two boundary layers must satisfy the stress balance condition (6) which yields

$$\mu_g U_g/\delta_g = \mu_l |U_l|/\delta_l \tag{15}$$

Together with (14) this equation fixes the ratio U_g/U_l. For realistic liquid-gas parameter values one finds $U_g \gg |U_l|$. When the Reynolds numbers are large the boundary layers grow slowly by diffusion.

The full, Navier–Stokes, viscous equations were perturbed to find a linearized approximation. The resulting Orr-Sommerfeld equations were solved using a polynomial expansion and standard linear algebra packages (Yecko *et al.*, 2002; Boeck & Zaleski, 2005). Comparison of full numerical simulations with the predictions of the Orr-Sommerfeld theory gave excellent agreement as shown on Figure 3 for parameter values $\mathrm{Re}_g(L) = 8000, r = 0.1, m = 0.02, \sigma = 0$. The boundary layer sizes were $\delta_l = \delta_g = L/4$. The computations reported in this Section were initialized using the linear mode computed from the Orr-Sommerfeld equation. Exponential growth was observed on a range of amplitudes of several orders of magnitude. Details of the analysis and numerical resolution of the linearized equations may be found in Yecko *et al.* (2002); Boeck & Zaleski (2005).

Another delicate point when performing a comparison between linear theory and simulations is the necessity to avoid artifacts at early times. At initial time the flow is set to the mode given by linear theory. The correct growth rate is embedded in this mode: indeed the initial velocity of the fluid under the interface in that mode is $v_0 = dh/dt(0) = h_0 s$ where s is the growth rate and h_0 the initial interface height. Thus the short-time dependence $h(t) = h_0 + h_0 st$ yields, still at short times, an apparent growth of the form $h = h_0 \exp(st)$. To avoid this type of artifact it is important to continue the simulation until h/h_0 has varied by several orders of magnitude, as we did in our comparisons. Moreover one of us (P.Y.) has also compared the full numerical solution starting from random initial perturbations, finding equally good agreement with Orr-Sommerfeld theory.

On Figure 4 a typical comparison is shown. On this figure and the following ones, h_1 is the Fourier amplitude of the interface deformation $h(x)$ with the minimal wavenumber $2\pi/L$. The amplitude of the perturbation starts at 10^{-6}, much smaller than the grid spacing. In order to compare with the most often used method, we have used the arithmetic mean. The initial growth is faster than the theory, but as the amplitude reaches the level of the grid spacing, the numerical and theoretical growth rates agree. When

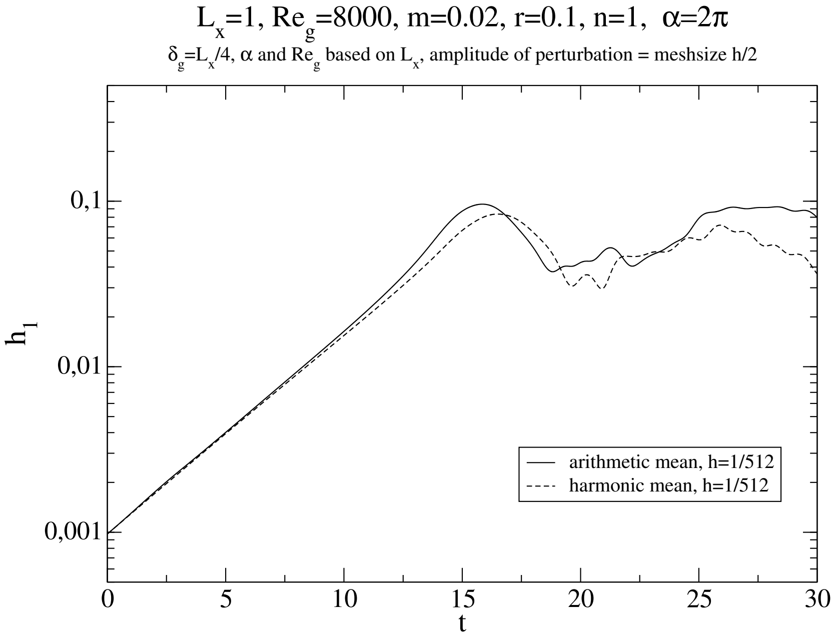

Figure 3: Amplitude growth for the arithmetic and harmonic mean of the viscosity with initial amplitude of the order of the mesh size. The numerically obtained amplitude growth is undistinguishable from the theoretical straight line obtained from the solution of the Orr-Sommerfeld equations in the early, linear part.

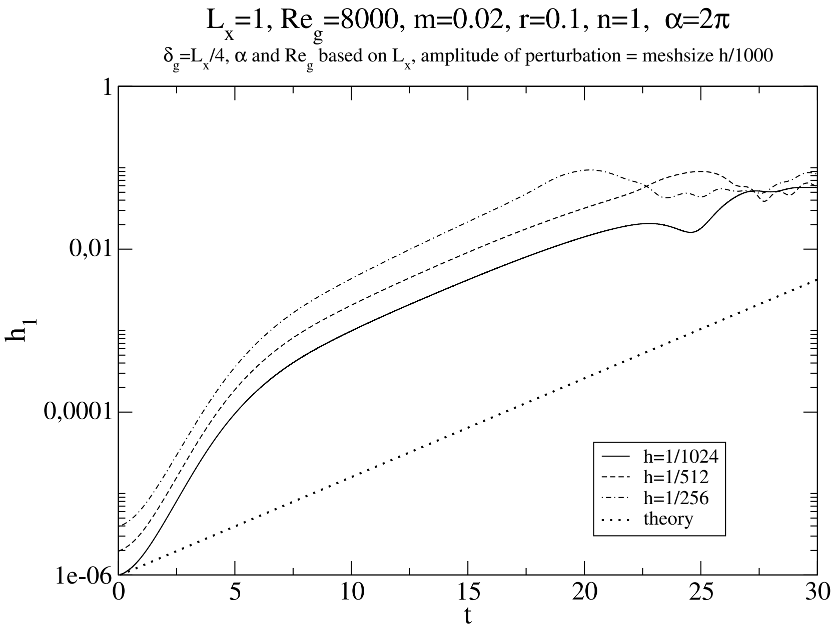

Figure 4: Amplitude growth for an unstable mode as a function of dimensionless time. Variables are dimensionless with the simulation box size L_x.

one uses the harmonic mean, the initial rapid growth phase does not show and the agreement with theory is immediate (Figure 5). Finally when the initial amplitude of the perturbation is large enough, there is no difference between the two methods (Figure 3).

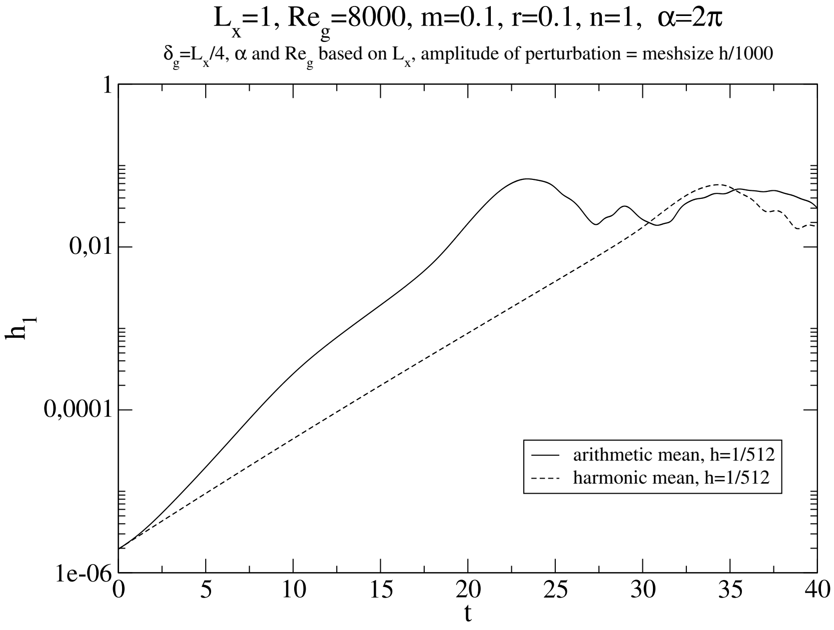

Figure 5: Amplitude growth for the arithmetic and harmonic mean of the viscosity with initial amplitude smaller than the mesh size.

There is a significant difference between the two methods, but it appears only when the deformations are smaller than the grid size. The harmonic mean is definitely preferred here, but we do not exclude that the arithmetic mean may be better in other flow configurations.

4 Nonlinear results

4.1 Initial conditions and simulation parameters

Initially, a liquid layer of thickness $L/3$ is placed at the bottom of a square $L \times L$ simulation domain, corresponding to an uniform square grid. The interface is flat at initial time while we used various profiles for the velocity. The instability is triggered by inserting two pairs of vortices inside the liquid phase. Therefore, the initial wavelength of the imposed instability is $\lambda = 0.5L$. The vortices are patches of uniform vorticity of radius $r_c = 4\,10^{-2}L$. Their dimensionless circulation (indicated in Table 1) is $\Gamma = (\oint u dl)/(2\pi \Delta U L)$, where ΔU is the velocity difference between gas and liquid. For two boundary layers $\Delta U = U_g + U_l$. In what follows we use dimensionless numbers $\mathrm{Re}_{l,g}, \mathrm{We}_{l,g}$ based on ΔU and L.

We have performed a very large number of simulations at various values of the parameters. There are however about eight independent parameters (Six in Table 1 and Re_l and r). A full parametric study as a function of the eight parameters is beyond the means of the present study, so we had to fix the values of some of the parameters. The overall principle guiding the choice of the parameter is numerical convenience: it is difficult to perform accurate simulations when the surface tension (dimensionless surface tension may be measured by the Laplace number $La = \rho_l d\sigma/\mu_l^2 = Re_l^2/We_l$ where d is a characteristic length scale.), the Reynolds numbers and the density ratio are all large. Although such computations are not impossible to attain, they are much more complex. The simulations in this paper are thus restricted to the case $r = 0.1$ which is simpler than the air-water one (which has $r \approx 0.0012$). This simpler case has however direct applications to liquid-gas atomization at high pressure. We let $\mathrm{Re}_l = 1000$ as this provides a low-enough liquid viscosity to diminish the effect of liquid viscosity on ligament formation. The other parameters varied are Re_g and We_g, and, in some cases, the boundary layer width and structure.

The initial boundary-layer configuration is delicate to fix. In all cases except D3 and E, the boundary layer widths are fixed by the diffusive growth condition (14). The ratio U_g/U_l is fixed by the stress balance condition (15).

4.2 Convergence study

The effect of grid resolution is a tricky issue that we discuss in this Section and in Section 4.8. On Figure 6 we show the result of a comparison between the two viscosity methods (harmonic and arithmetic) and for two grid sizes. The parameters are those of case D in Table 1.

We see that convergence is attained in both cases, and that the choice of the viscosity method has no visible effect. On the other hand when we initialize the simulation with an initial sharp velocity profile as shown in Fig. 2(a) (a simplification used in most simulations of the literature for the sake of simplicity) we see two effects on Fig. 7. One is that as the grid is refined, more and more small structures are seen. The other effect is that these small structures are more pronounced in the arithmetic mean case. A likely explanation for the small structures is as follows: the case of a sharp velocity profile is essentially identical to a profile where the boundary layers have shrunk to the size of the grid spacing. As the boundary layers decrease in size, the modes found by the Orr-Sommefeld theory (Boeck & Zaleski, 2005) reach a very large growth rate and wavenumber. This can be seen by comparing Fig. 19 and Fig. 22 containing the growth rates for the cases D and D2. For the second effect, the growth is enhanced in the arithmetic mean case as it gives faster growth in the initial instants as on Fig. 4.

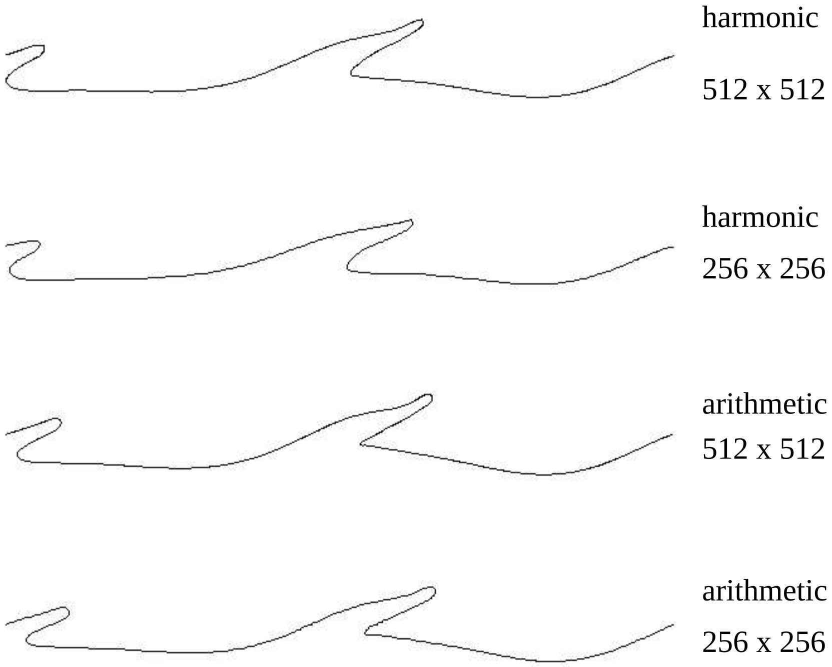

Figure 6: Nonlinear development of the instability for the two viscosity methods and two grid sizes (case D).

Table 1: Parameters used in the unequal density simulations. None instead of a value for $\delta_{l,g}/L$ means that there were no boundary layers. Numbers $\mathrm{Re}_g^\star$, $\mathrm{We}_g^\star$ are based on boundary layer sizes.

Run	$\mathrm{Re}_g(L)$	$\mathrm{We}_g(L)$	μ_g/μ_l	δ_g/L	δ_l/L	Γ	$\mathrm{Re}_g^\star$	$\mathrm{We}_g^\star$
A	500	500	0.2	0.1	0.707	0.075	43.81	38.38
B	4000	500	0.025	0.1	0.2	0.025	380.95	45.35
C	500	4000	0.2	0.1	0.707	0.025	43.81	307.02
D	4000	4000	0.025	0.1	0.2	0.025	380.95	362.81
D1	4000	4000	0.025	0.1	0.2	0.05	380.95	362.81
D2	4000	4000	0.025	0.01	0.02	0.05	38.1	36.28
D3	4000	4000	0.025	0.1	inverted b. l. (see text)			
E	4000	4000	0.025	none	none	0.025	—	—

From these results, we conclude that the initial sharp velocity profile (Figure 2(a)) is an ill-posed problem: ever faster growth rates are obtained as the grid is refined and larger wavenumber are explored. Thus in what follows we always initialize the flow with small boundary layers in *both the gas and in the liquid.*

4.3 Ligament formation at balanced density

Before we move on to the solution of the full problem, it is interesting to consider a simpler case. We performed simulations with equal viscosity and densities, and a sharp velocity jump. Typical Kelvin-Helmholtz roll-ups are obtained, with the two phases occupying symmetrical regions of space. However if the base flow is made asymmetrical with a boundary layer in the gas only then the flow of Figure 8 is observed. In that case, the boundary layer

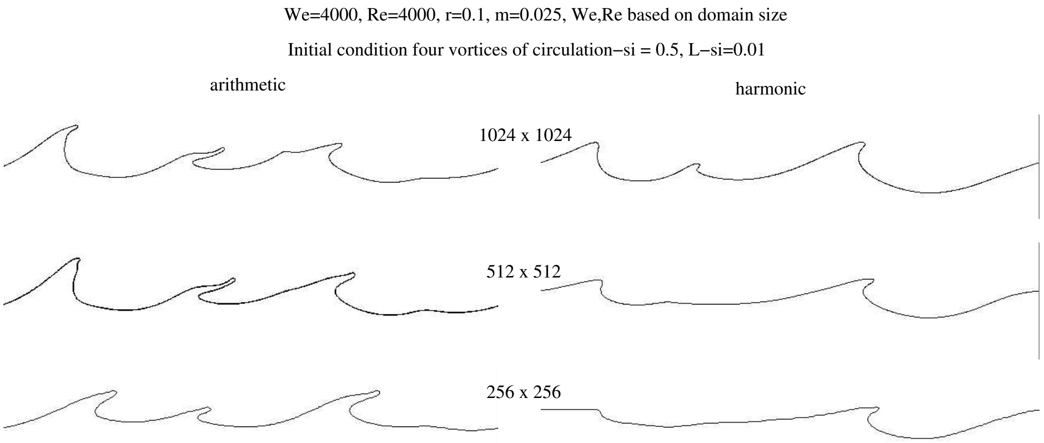

Figure 7: Nonlinear development of the instability for the two viscosity methods and for two grid sizes (case E).

was linear as in Figure 2(b) with no boundary layer in the liquid ($U_l = 0$) and $\delta_g = 0.2L$, $\mathrm{Re}_l = \mathrm{Re}_g = 2000$, $\sigma = 0$. Grid size was 256×256 nodes. Notice how a ligament-like structure forms at $t = 1$. This demonstrates that density or viscosity asymmetry are not alone responsible for the asymmetric ligament formation: the asymmetry in boundary layers plays a major rôle. Such an asymmetry in boundary layers occurs in most realistic flows. As a result of the stress-balance condition (15) $U_g/U_l = \mu_l/\mu_g(\nu_g/\nu_l)^{1/2}$. The right-hand side is a large number for most fluids, and thus most of the vorticity is in the gas.

4.4 Results for variable density

We have observed ligament formation and evolution in the non-linear regime. Ligaments form if Re_g, We_l and Γ are all large enough as shown on diagram 9 (This diagram was completed at relatively low resolution, thus the results

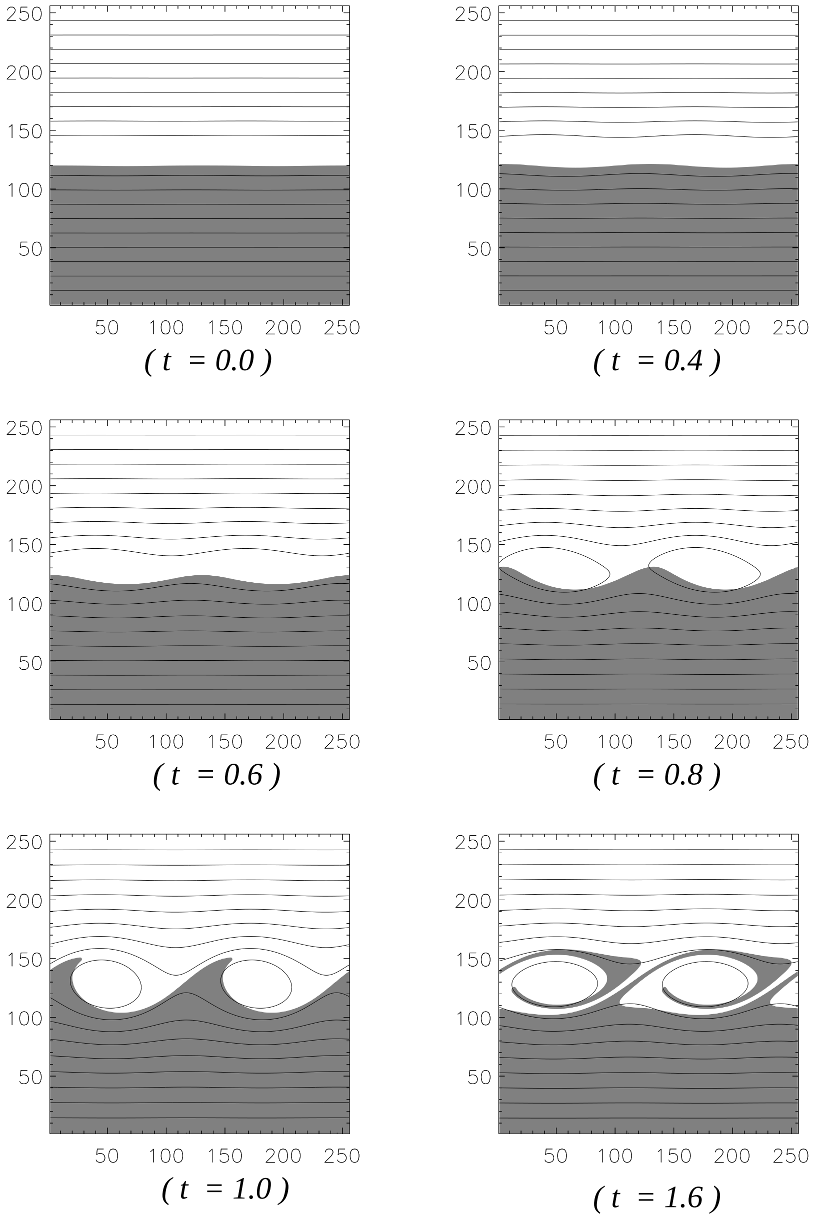

(t = 0.0)

(t = 0.4)

(t = 0.6)

(t = 0.8)

(t = 1.0)

(t = 1.6)

Figure 8: Simulation of a sheared flow between identical fluids. There is no surface tension. The only asymmetry is in the boundary layers, as described in the text. The lines are streamlines and the grey area tracks the “liquid” phase. The gas boundary layer is visible as the region where streamlines are more sparse.

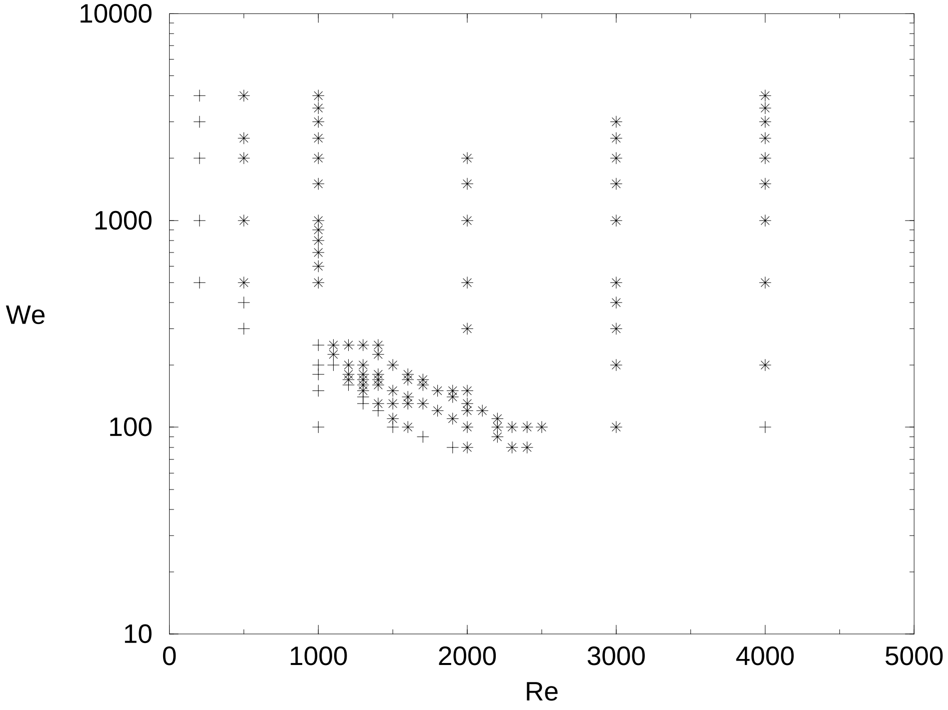

Figure 9: Diagram in parameter space showing when ligaments form and eventually break at low (256 × 256 resolution. Symbols $*$ indicate that a ligament formed and broke, while $+$ symbols indicate that ligaments did not fully develop)

are not readily comparable to those of Figures 11, 14, 17 etc.). A discussion of the limits in this diagram is given in the next Section.

Four stages in the simulated development may be identified, although not all of them occur for all parameter values. (i) The interface deforms with a steadily growing amplitude. Vorticity remains attached close to the interface but the gas boundary layer grows more or less rapidly depending on Reynolds number. This stage corresponds to the linear development of the instability as well as the early nonlinear development. (ii) Vorticity detaches from the boundary layers. This corresponds to the situation at $t = 0.8$ on Figure 8. (iii) Ligaments form. In the symmetric fluids case this is the situation at $t = 1$. Various ligament shapes are shown on Figures 11, 14, 17, 20, 21. (iv) As the ligaments stretch and bend, their tips grow into a more or less visible bulge or end rim from capillary effects. This rim is of the type studied by Taylor (1959); Culick (1960). It was shown by Brenner & Gueyffier (1999) that it is more or less rounded depending on the ratio of viscous to surface tension forces. The 3D destabilization of this rim is one of the possible mechanisms for droplet formation (Fullana & Zaleski, 1999).

A wider rim is most clearly seen when the Weber number is relatively moderate as on Figure 11(b). Behind the thick rim the ligament continues to stretch and eventually becomes so thin that it breaks. This rupture is a resolution-dependent phenomenon.

We have frequently observed between step (ii) and (iii) that vortices merge, ending with a single ligament and a single vortical region. This vortex merging phenomenon is consistent with the vortex merging observed in the spatial development of shear layers (Brown & Roshko, 1974). Indeed Raynal (1997) has observed an increase in the wavelength with the distance from the nozzle. This overall picture is modified with the parameters of the flow in a way we shall now examine.

4.5 Effect of Reynolds and Weber numbers

Table 1 describes the cases simulated in the nonlinear regime. It contains four basic cases A, B, C and D and a few others derived from the basic cases. To build these cases, we consider two values of the gas Reynolds and Weber numbers: a “small” value of 500 and a “large” value of 4000 and get four combinations. The growth rates predicted for five of the cases by the Orr-Sommerfeld theory are shown on Figures 10-22. These show the growth rate αc_i as a function of α, the wavenumber of the unstable mode; c_i is the imaginary part of the wave speed. The observed stability of the flow is however not immediately derived from the theoretical growthrates. This is because the base flow is not “frozen” as time increases, the boundary layer size increases as $\sqrt{\nu t}$. Thus an initially unstable configuration may become stable. The time scale for boundary layer growth for phase p is $t_\nu = \delta_p^2/\nu_p$ and the time scale for instability is $t_i = L\alpha c_i/\Delta U$. The ratio of the time scales is $R_p = t_\nu/t_i = \alpha c_i \mathrm{Re}_p^* \delta_p/L$, where Re_p^* is the Reynolds number based on boundary layer size and other quantities in phase p. To maintain the profile approximately “frozen” in both layers during the growth of the instability by several e-folds one needs to have both $R_g, R_l >> 1$. A similar theory was put forward by Villermaux (1998) and Raynal (1997) but based on the inviscid linear theory alone. In the inviscid theory, there is only one unstable mode which as a rule of thumb is less unstable than the viscous modes as shown by Boeck & Zaleski (2005).

The lowest Re and We numbers are those of case A, for which simulations were performed with resolution up to 1024×1024. One sees from Table 1 and Figure 10 that the $n = 2$ mode, which corresponds to the initialization

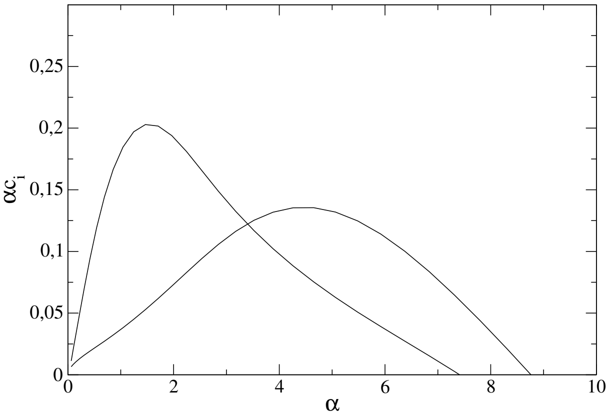

Figure 10: The growth rates in linear Orr-Sommerfeld theory for case A. The wavenumber α is in units of $1/L$. Thus the wavenumbers that fit in the box are $\alpha = 2n\pi$. Only the $n = 1$ mode is unstable, while our initial condition with two pairs of vortices corresponds to $n = 2$ and a stable mode. Both the standard mode and the H-mode are seen in this case.

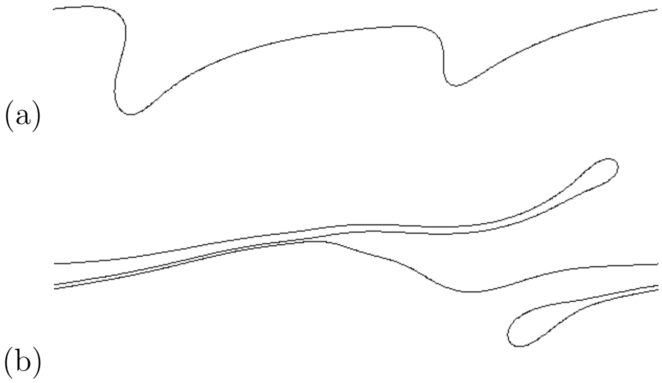

Figure 11: Two stages of ligament formation and elongation at low Reynods number, 512×512 grid, case A $\mathrm{Re}_g = 500$ and $\mathrm{We}_g = 500$, (a) $t = 2.8$ (b) $t = 7.92$.

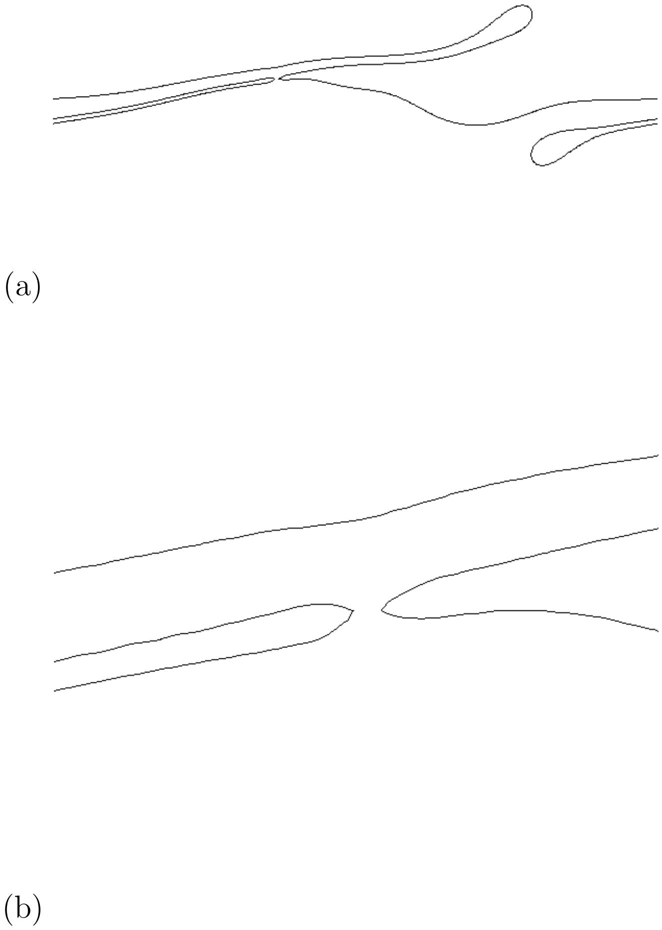

Figure 12: Reconnection of the thin gas layer in the simulation case A with filtered C in the surface tension method (equation (12)), at time $t = 7.28$. (a) full domain (b) detail.

by our four vortices, is stable. However non-linear interaction will also excite mode $n = 1$ with wavenumber $\alpha = 2\pi$, which is barely unstable (Figure 10) for which $R_g \simeq 0.4$. So despite the apparently high We and Re numbers for case A the conditions for instability are not met. Indeed case A lies just on the edge of the ligament-forming region on Figure 9. Actually, case A is marked as "ligament-forming" on Figure 9, which reports results at resolution 256×256 with a moderate initial perturbation ($\Gamma = 0.025$), while the sequence obtained at resolution 512×512 and higher with a similar moderate initial perturbation does not lead to fully formed ligaments and breakup.

It is interesting to notice that the instability in cases A and C would be even weaker, but for the existence of the second instability mode. This shows the importance of computing accurately the stability properties in the realistic viscous framework. Nonlinear calculations show that ligaments form in a transient way but subsequently not stretch sufficiently to eventually fracture, even at moderate resolution. However, with a relatively large circulation in the initial condition ($\Gamma = 0.075$), one does see the formation of a ligament, with a relatively large end rim. For such a large initial circulation the early non linear shapes differ from those obtained with smaller amplitude vortices (for instance in Figure 6). The air forms fingers entering the liquid (Figure 11(a)). An interesting effect of the surface tension algorithm may be observed. On Figure 12 we see that using the filtered C for surface tension creates an attractive force between the interfaces that speeds up the reconnection. This may be understood as the filtering will "feel" the neighboring interface at a longer distance. In some sense it makes the interface thicker from the point of view of the surface tension method. Without filtering, a similar reconnection also occurs but much later, at $t = 8.8$.

Case C has the same moderate Re but larger We. A thinner, longer ligament is created (Figure 14), at the standard value of the circulation. We show on Figure 14c the last image before reconnection occurs: in a manner similar to case

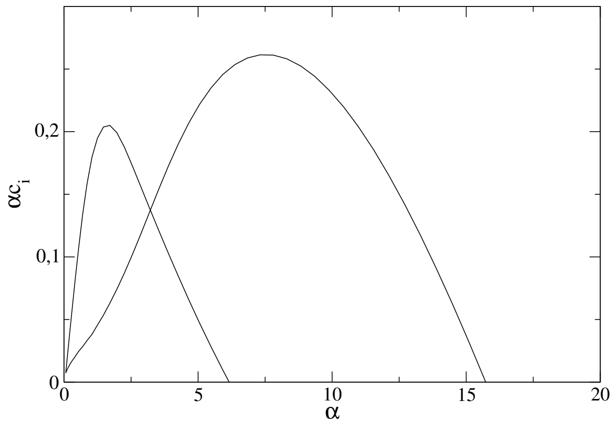

Figure 13: The growth rates in linear Orr-Sommerfeld theory for case C. Two modes are seen again.

If we increase the Reynolds number but keep the Weber number moderate as in case B we obtain the sequence shown in Figure 17. It is seen that the two bumps merge between times $t = 4$ and $t = 4.8$. At $t = 9.76$, just before breakup a very long ligament is seen (the reader should remember that the domain is periodic, and lines ending on the right are connected to lines starting on the left; thus on Figure 17c a single ligament winds around the periodic box). The complex shape observed at time 9.76 is created by a process of folding and stretching.

Finally, if we increase the Reynolds number and the Weber number as in case D the ligament folds again in complex ways as show on Figure 20.

The effect of the gas Reynolds number on the stretching and fracture mechanism can be seen by comparing the results for the low Reynolds number cases A and C with those of the higher Reynolds numbers cases B and D.

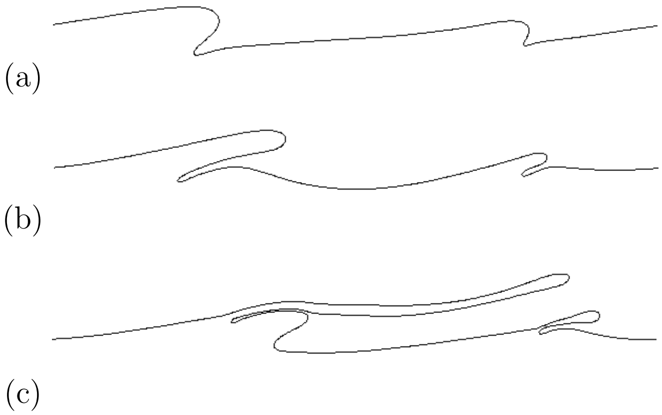

Figure 14: Three stages of ligament formation and elongation at low Reynods number, 512×512 grid, case C $\mathrm{Re}_g = 500$ and $\mathrm{We}_g = 4000$, (a) $t = 4$ (b) $t = 5.6$ (c) $t = 8.8$.

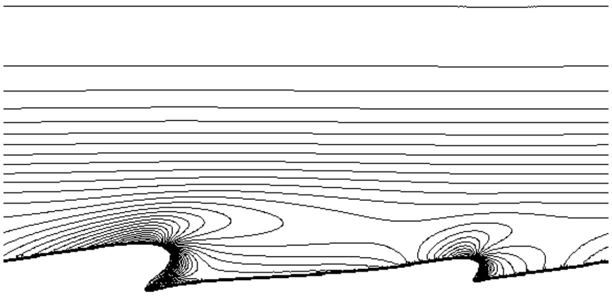

Figure 15: Vorticity in case C at $t = 4$

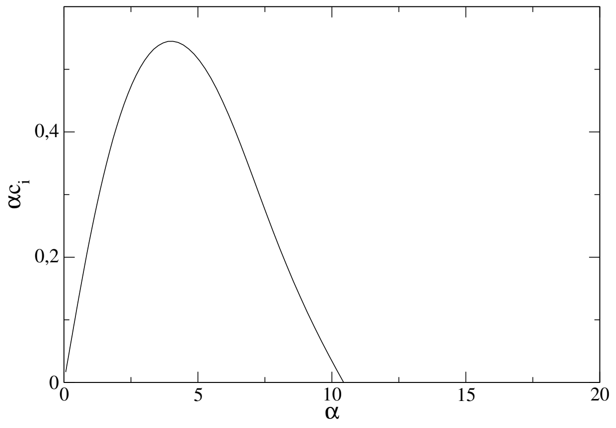

Figure 16: The growth rates in linear Orr-Sommerfeld theory for case B.

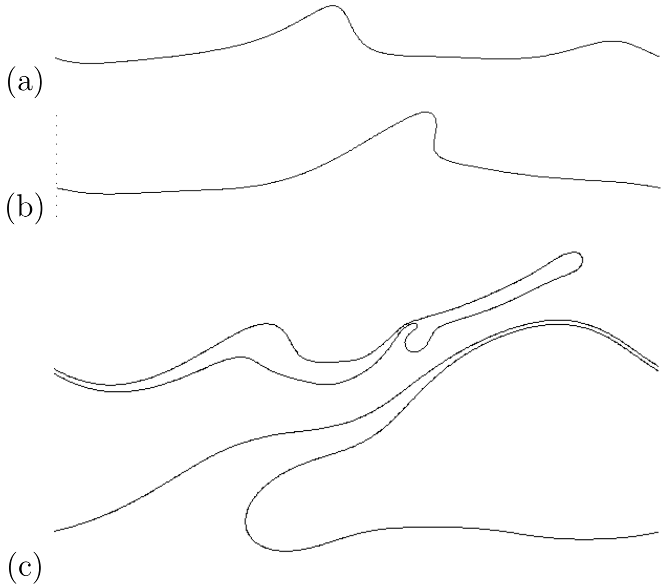

Figure 17: Three stages of ligament formation and elongation at higher Reynods number, 512×512 grid, case B: $\mathrm{Re}_g = 4000$ and $\mathrm{We}_g = 500$, (a) $t = 4$ (b) $t = 4.8$ (c) $t = 9.76$.

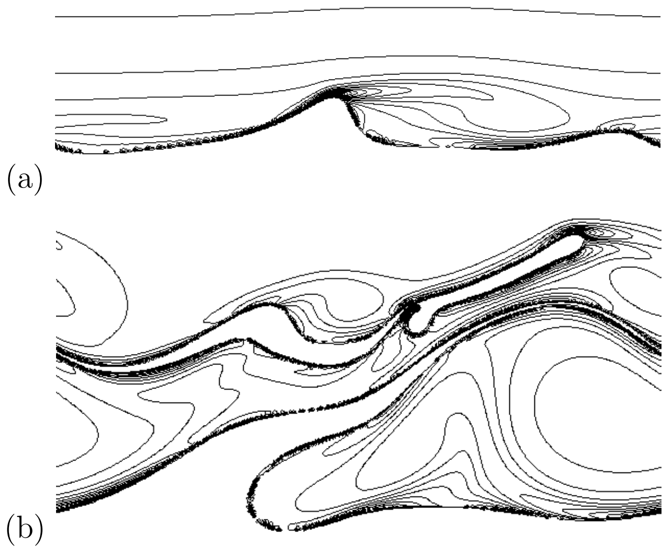

Figure 18: Vorticity in case B at (a) $t = 4$ and (b) $t = 9.76$

At relatively low Reynolds number (near the left boundary in Figure 9) the boundary layer $\delta_g(t)$ grows fast. Before the ligaments have fully developed, the boundary layer has spread over the entire box and little vorticity is left. This may be seen on Figure 15 which shows the vorticity contours for case C. At higher Reynolds number, vorticity does not spread but detaches from the ligaments as shown in Figure 18. This process of boundary layer separation, or roll-up, may occur very early. At high Reynolds numbers even a small deformation of the interface triggers separation and roll up.

The effect of the Weber number may also be inferred from these results. As a rough guide, a large Weber number favors the formation of very thin ligaments with almost negligible end rims. However the time at which the ligament is observed is also relevant. When breakup occurs late, ligaments had the time to thin in their central part but the end rims have grown. This may be seen for instance on Figure 14c: although the Weber number is rather large, a significant end rim is seen.

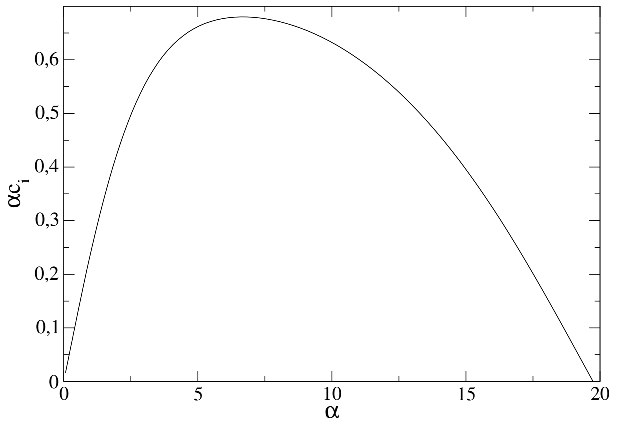

Figure 19: The growth rates in linear Orr-Sommerfeld theory for case D.

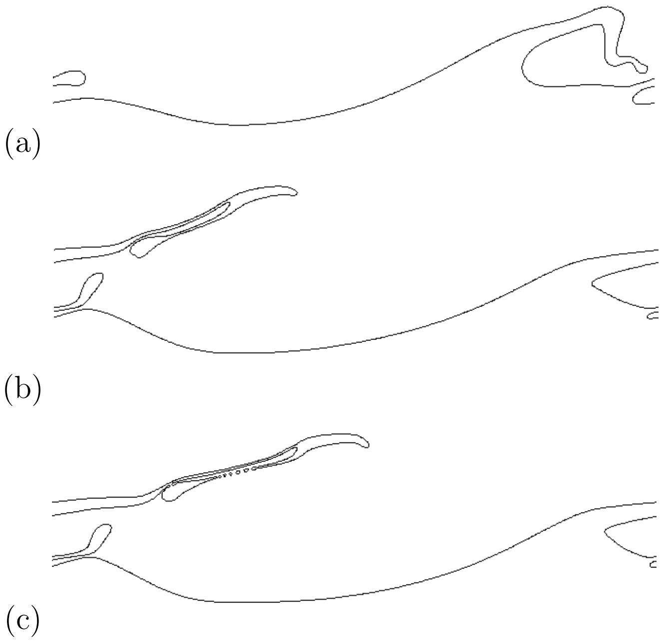

Figure 20: Three stages of ligament formation and elongation at higher Reynods number, 512×512 grid, case D $\mathrm{Re}_g = 4000$ and $\mathrm{We}_g = 4000$, (a) $t = 6$ (b) $t = 6.8$ (c) $t = 6.96$.

4.6 Effect of the perturbation amplitude

One effect of a large perturbation amplitude has already been seen in case A: the air penetrates the liquid.

In the high Reynolds number case, varying the initial amplitude of the perturbation also has a dramatic effect on the fate of the ligament. Increasing the initial perturbation, as in Case D1, makes the ligament rapidly sprout up. A thin ligament, pointing upwards, is formed. It is shown just before its breakup (at time $t = 4$) on Figure 21.

Which amplitude for initial perturbations is realistic depends on the experiment or natural configuration being considered. While some nozzles will involve highly turbulent flow, others are controlled to reduce the level of turbulence in the nozzle. The turbulence level, defined as the ratio of root mean square fluctuating velocity to the mean flow velocity may arguably be of the order of Γ, and turbulence levels of 0.01 are not uncommon.

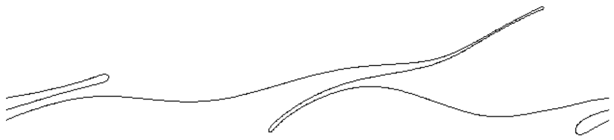

Figure 21: Case D1 (same as D but at larger perturbation amplitude): the breakup occurs much earlier, just after time $t = 4$, which is shown here.

4.7 Effect of the boundary layers

All the simulations we have shown up to now involve boundary layers of the shape shown on Figure 2(c), obey the condition of diffusive growth of the boundary layers (14) and have the same width in the gas layer. We

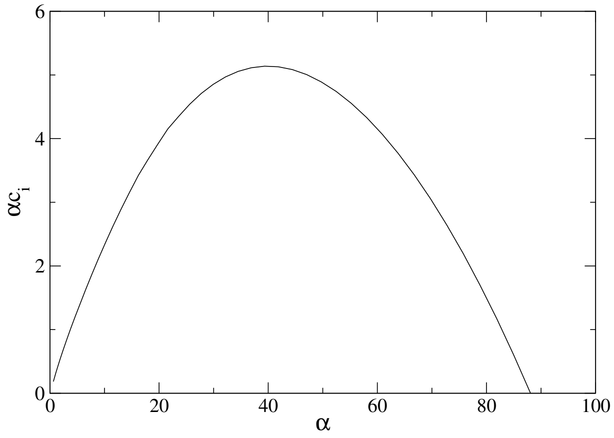

Figure 22: The growth rates in linear Orr-Sommerfeld theory for case D2.

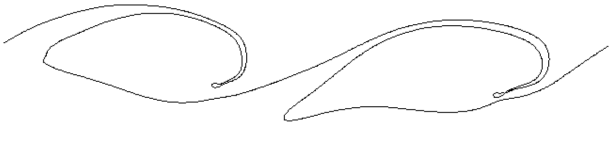

Figure 23: Case D2 : larger perturbation amplitude but thinner boundary layers. At time $t = 2.4$ the ligaments roll up instead of shooting upwards.

have attempted many simulations were one or several of these conditions are modified. This usually changes the eventual fate of the ligament. For instance, thinner boundary layers change case D1, in which the ligament was pointing upwards before breakup, into ligaments rolling downwards (Figure 23). The result for these thin boundary layers is however different from the result obtained with no boundary layers (case E, not shown for late times).

Finally we have attempted to simulate the kind of boundary layers that would occur just downstream of the splitter plate between parallel liquid and gas streams. In that case, just behind the splitter plate, the boundary layers will have the shape shown on Figure 2(d). In case D3 liquid velocity is now of opposite sign

$$u_{0,l}(y) = -U_l \mathrm{erfc}\left(\frac{y}{\delta_l}\right). \tag{16}$$

In case D3, the parameters are identical to case D but the condition of stress balance (15) cannot be verified. The liquid velocity is set instead arbitrarily by $U_l/U_g = 0.1$ (a realistic ratio for laboratory experiments). We now find again a ligament pointing rapidly upwards.

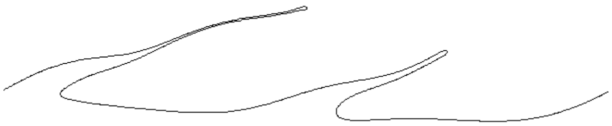

Figure 24: Case D3 : Inverted liquid boundary layer. At time $t = 4.48$ the left ligament points up and is about to break.

4.8 Effect of grid resolution

One effect of grid resolution that we have already reported is that coarse grids lead to stronger instability : for instance in case A ligaments form at 256×256 as shown in Figure 9 while ligaments do not form at higher resolution. This is due to a lower effective surface tension at low resolution. Once instability is set and ligaments are stretching, finer grids lead to later breakups, however the process is not uniform. At some moments and locations in the flow, the ligaments are caught in rapid elongational flows that break them rapidly no matter what the resolution. Then increasing the resolution has no dramatic effect. For most of the figures shown, varying the resolution between 256^2 and 1024^2 has no qualitative effect. On the other hand, in some cases a remarkable effect is seen. On Figure 25 we show case B at low resolution, just before breakup. In a sense, this lower resolution simulation may look more realistic compared to experimental photographs: this may be because the thinner, longer, convoluted ligaments obtained at larger resolution are often broken by three-dimensional effects.

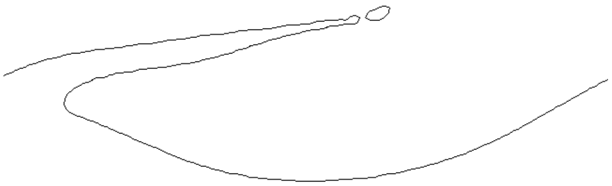

Figure 25: Case B at lower resolution: the breakup occurs much earlier than in the high resolution case. Here the ligament is shown at $t = 8.4$ just before breakup.

5 Conclusion

In the foregoing, we have described a method built on several known numerical schemes, such as Volume of Fluid, which together allow the deformation of interfaces in a mixing layer to be followed. The validation is performed through comparisons with the linear theory. In this way a kind of cross-validation is achieved: the linear theory, which is rather complex, is also made more reliable through the agreement with the full numerical resolution of the Navier-Stokes equations.

We also show that the method used to approximate the viscous terms in the mixed cells may have an important effect on the growth rate, but the effect is limited to the range where the perturbation ampliture is small relative to the grid size. Nevertheless, this effect may over-amplify the growth of some length scales if proper care is not taken.

Indeed, our results show that one ingredient of a careful treatment of the instability is the introduction of boundary layers in the initial conditions. The absence of initial boundary layers makes the problem ill-posed because of the appearance of very rapidly growing modes. This results in poor convergence as the grid is refined.

On this basis we have been able to obtain some results on the non-linear development of the instability. One of the most striking effects is that relatively large Reynolds and Weber numbers are necessary to observe growing ligaments. Going further in time after the formation of the ligaments, one eventually sees the topology of the solutions change. This event is dependent on the grid resolution and thus difficult to analyze. Physical reality is three-dimensional and because of this the real flows may diverge from the solutions in this paper before the breakup stages we have identified actually occur. On the other hand, in a fast flow the width of the sheets may become so thin, of the order of nanometers, that they would break physically (see Raynal (1997) pp 196 and 198 for experimental evidence).

Nevertheless the simulations show realistic mechanisms and may be used to build theories of droplet formation. A systematic prediction of the size of the end rim may help in determining the final droplet size. As seen in this paper, accurate predictions require very high resolution simulations. A complete series of such simulations should be undertaken to determine end-rim size as a function of physical parameters.

Another perspective of this work is to perform three-dimensional and spatially developing simulations of comparable resolution. Most existing three-dimensional work, including the work by some of us (for instance Zaleski *et al.* (1996); Bianchi *et al.* (2005)) suffers from one or several defects that we tried to avoid in the present work: resolution too small (i.e. grids too coarse), initial perturbation amplitude too large, lack of boundary layers. Correcting these defects is likely to require extensive computing resources, even allowing for a future marked increase in computer power.

Another perspective is to extend these results to more realistic cases, were the parameters are closer to the experimental conditions of an air-water experiment in a laboratory or a wind generated wave in the natural environment. Such a study would involve more numerical difficulties than the present one, as it requires to increase both the surface tension (or the number La) and the density ratio. It would however be of considerable interest.

Acknowledgements

Support for the early part of this work was provided by the P.R.C moteurs fusées, the G.D.R. moteurs fusées, Société Européenne de Propulsion (now a division of SAFRAN), the Centre National d'Etudes Spatiales (C.N.E.S.) and the Centre National de la Recherche Scientifique (C.N.R.S.). In the past three years support was provided by C.N.R.S. and the Deutsche Forschungsgemeinschaft (D.F.G.) under grant Bo 1668/2-1, which we gratefully acknowledge.

References

Aulisa, E., Manservisi, S., Scardovelli, R. & Zaleski, S. 2003 A geometrical area-preserving volume of fluid method. *J. Comput. Phys* **192**, 355–364.

Bianchi, G. M., Pelloni, P., Toninel, S., Scardovelli, R., Leboissetier, A. & Zaleski, S. 2005 A quasi-direct 3D simulation of the atomization of high-speed liquid jets. In *Proceedings of ICES05, 2005 ASME ICE Division Spring Technical Conference*. Chicago, Illinois, USA, April 5-7, 2005.

Boeck, T. & Zaleski, S. 2005 Viscous versus inviscid instability of two-phase mixing layers with continuous velocity profile. *Phys. Fluids* **17**, 032106.

Brenner, M. & Gueyffier, D. 1999 On the bursting of viscous films. *Phys. Fluids* **11**, 737–739.

Brown, G. L. & Roshko, A. 1974 On density effects and large structure in turbulent mixing layers. *J. Fluid Mech.* **64**, 775–816.

Chandrasekhar, S. 1961 *Hydrodynamic and Hydromagnetic Stability*. Oxford Univ. Press.

Culick, F. E. C. 1960 Comments on a ruptured soap film. *J. Appl. Phys.* **31**, 1128–1129.

Faeth, G., Hsiang, L.-P. & Wu, P.-K. 1995 Structure and breakup properties of sprays. *Int. J. Multiphase Flow* **21**, 99–127, supplement issue.

Fullana, J. M. & Zaleski, S. 1999 Stability of a growing end-rim in a liquid sheet of uniform thickness. *Physics of Fluids* **11**, 952–954.

Gordillo, J. M. & Perez-Saborid, M. 2005 On the first wind atomization regime. *J. Fluid.Mech* **541**, 1–20.

Gueyffier, D., Nadim, A., Li, J., Scardovelli, R. & Zaleski, S. 1999 Volume of fluid interface tracking with smoothed surface stress methods for three-dimensional flows. *J. Comput. Phys.* **152**, 423–456.

Hinch, E. 1984 A note on the mechanism of the instability at the interface between two shearing fluids. *J. Fluid Mech.* pp. 463–465.

Hooper, A. P. 1985 Long-wave instability at the interface between two viscous fluids: Thin layer effects. *Physics of Fluids* **28** (6), 1613–1618.

Hooper, A. P. & Boyd, W. G. C. 1983 Shear-flow instability at the interface between two viscous fluids. *J. Fluid Mech.* **128**, 507–528.

Hooper, A. P. & Boyd, W. G. C. 1987 Shear-flow instability due to a wall and a viscosity discontinuity at the interface. *J. Fluid Mech.* **179**, 201–226.

Hoyt, J. W. & Taylor, J. 1977 Waves on water jets. *J. Fluid Mech.* **83**, 119–127.

Keller, F. X., Li, J., Vallet, A., Vandromme, D. & Zaleski, S. 1994 Direct numerical simulation of interface breakup and atomization. In *Proceedings of ICLASS94* (ed. A. J. Yule), pp. 56–62. New York: Begell House.

Lafaurie, B., Nardone, C., Scardovelli, R., Zaleski, S. & Zanetti, G. 1994 Modelling merging and fragmentation in multiphase flows with SURFER. *J. Comput. Phys.* **113**, 134–147.

Lasheras, J. C. & Hopfinger, E. J. 2000 Liquid jet instability and atomization in a coaxial gas stream. *Annu. Rev. Fluid Mech.* **32**, 275–308.

Leboissetier, A. & Zaleski, S. 2002 Influence des conditions amont turbulentes sur l'atomisation primaire. *Combustion (Revue des Sciences et Techniques de Combustion)* **2**, 75–87.

Lefebvre, A. H. 1989 *Atomization and Sprays*. Taylor & Francis.

Li, J. 1995 Calcul d'interface affine par morceaux (piecewise linear interface calculation). *C. R. Acad. Sci. Paris, série IIb, (Paris)* **320**, 391–396.

Marmottant, P. & Villermaux, E. 2002 Atomisation primaire dans les jets coaxiaux. *Combustion (Revue des Sciences et Techniques de Combustion)* **2**, 89–126.

Rangel, R. & Sirignano, W. 1988 Nonlinear growth of Kelvin–Helmholtz instability: effect of surface tension and density ratio. *Phys. Fluids* **31**, 1845–1855.

Raynal, L. 1997 Thèse. PhD thesis, Universite Joseph Fourier, Grenoble.

Reitz, D. & Bracco, F. 1982 Mechanism of atomisation of a liquid jet. *Physics of Fluids* **25**, 1730–1742.

Scardovelli, R. & Zaleski, S. 1999 Direct numerical simulation of free-surface and interfacial flow. *Annu. Rev. Fluid Mech.* **31**, 567–603.

Scardovelli, R. & Zaleski, S. 2003 Interface reconstruction with least-square fit and split lagrangian-eulerian advection. *Int J. Numer. Meth. Fluids* **41**, 251–274.

Tauber, W. & Tryggvason, G. 2002 Direct numerical simulation of primary breakup. *Comput. Fluid Dynamics J.* **9**.

Tauber, W., Unverdi, S. O. & Tryggvason, G. 2002 The non-linear behavior of a sheared immiscible fluid interface. *Phys. Fluids* **14**, 2871.

Taylor, G. I. 1959 The dynamics of thin sheets of fluid III. Disintegration of fluid sheets. *Proc. Roy. Soc. London A* **253**, 313–321.

Villermaux, E. 1998 On the role of viscosity in shear instabilities. *Phys. Fluids* **10**, 368–373.

Yecko, P., Zaleski, S. & Fullana, J.-M. 2002 Viscous modes in two-phase mixing layers. *Phys.Fluids* **14**, 4115–4122.

Zaleski, S., Li, J., Scardovelli, R. & Zanetti, G. 1995 Flows with interfaces: dealing with surface tension and reconnection. In *Proceedings of the IMACS-COST Conference on Computational Fluid Dynamics, Lausanne Sept. 13-15, 1995,Notes on Numerical Fluid Mechanics*. Vieweg, 53.

Zaleski, S., Li, J., Scardovelli, R. & Zanetti, G. 1996 Direct simulation of multiphase flows with density variations. In *IUTAM colloquium "Variable Density Low Speed Turbulent Flows"*. Kluwer.